HHS Public Access

Author manuscript

Ultrasound Med Biol. Author manuscript; available in PMC 2022 July 01.

Published in final edited form as:

Ultrasound Med Biol. 2021 July ; 47(7): 1670–1680. doi:10.1016/j.ultrasmedbio.2021.02.006.

Prostate Cancer Detection Using 3D Shear Wave Elasticity Imaging

D. Cody Morris[a,*], **Derek Y. Chan**[a], **Mark L. Palmeri**[a], **Thomas J. Polascik**[b], **Wen-Chi Foo**[c], **Kathryn R. Nightingale**[a]

[a]Department of Biomedical Engineering, Duke University, Durham, NC, USA

[b]Department of Surgery, Duke University Medical Center, Durham, NC, USA

[c]Department of Pathology, Duke University Medical Center, Durham, NC, USA

Abstract

Transrectal ultrasound (TRUS) B-mode imaging provides insufficient sensitivity and specificity for prostate cancer (PCa) targeting when used for biopsy guidance. Shear wave elasticity imaging (SWEI) is an elasticity imaging technique which has been commercially implemented and is sensitive and specific for PCa. We have developed a SWEI system capable of 3D data acquisition using a dense acoustic radiation force (ARF) push approach which leads to enhanced shear wave signal-to-noise ratio (SNR) compared to the commercially available SWEI systems and facilitates screening the entire gland prior to biopsy. Additionally, we imaged and assessed 36 patients undergoing radical prostatectomy using 3D SWEI and determined a shear wave speed (SWS) threshold separating PCa from healthy prostate tissue with sensitivities and specificities akin to multiparametric magnetic resonance imaging fusion biopsy. The approach measured the mean SWS in each prostate region to be: 4.8 m/s (Young's modulus E = 69.1 kPa) in the peripheral zone (PZ), 5.3 m/s (E = 84.3 kPa) in the central gland (CG), and 6.0 m/s (E = 108.0 kPa) for PCa with statistically significant ($p<0.0001$) differences among all regions. 3D SWEI ROC analyses identified a threshold of 5.6 m/s (E = 94.1 kPa) to separate PCa from healthy tissue with a sensitivity, specificity, PPV, NPV, and AUC of 81%, 82%, 69%, 89%, and 0.84, respectively. Additionally, a SWS ratio was assessed to normalize for tissue compression and patient variability which yielded a threshold of 1.11 to separate PCa from healthy prostate tissue and was accompanied by a substantial increase in specificity, PPV, and AUC, where the sensitivity, specificity, PPV, NPV, and AUC were 75%, 90%, 79%, 88%, and 0.90, respectively. This work demonstrates the feasibility of using 3D SWEI data to detect and localize PCa and demonstrates the benefits of normalizing for applied compression during data acquisition for use in biopsy targeting studies.

[*]Corresponding Author: D. Cody Morris, Room 1427, Fitzpatrick Center (FCIEMAS), 101 Science Drive, Campus Box 90281, Durham, NC 27708-0281; cody.morris@duke.edu; Phone, 919-660-5223.

Conflict of Interest

Authors K. Nightingale and M. Palmeri have intellectual property related to radiation force-based imaging technologies that has been licensed to Siemens, Samsung, and MicroElastic Ultrasound Systems.

Keywords

Prostate Cancer; Elasticity Imaging; Shear Wave Elasticity Imaging; Acoustic Radiation Force Impulse Imaging

Introduction

Prostate cancer (PCa) will lead to an estimated 191,930 new cancer diagnoses and 33,330 deaths in the United States in 2020 (Siegel et al., 2020). While this is the most common non-skin cancer diagnosis, it is the second most common cause of cancer related death for men, behind lung cancer (Siegel et al., 2020). The prevalence of PCa increases with age and ranges from 1.8% of men developing PCa before age 59 and 11.6% of men developing PCa over the course of their entire life (Siegel et al., 2020). Historically PCa screening has been performed using a digital rectal exam (DRE) and prostate-specific antigen (PSA) test, where a suspicious DRE or an elevated PSA (>4.0 ng/mL) would lead to a follow-up transrectal ultrasound (TRUS) guided biopsy. TRUS guided biopsy commonly consists of 10-12 biopsy cores sampled throughout the prostate where B-mode ultrasound is used to guide the biopsy needle to specific regions of the prostate (Mottet et al., 2017). This form of prostate biopsy has reported sensitivities and specificities ranging from 39-75% and 40-82%, respectively (Heijmink et al., 2011; Postema et al., 2015). As only 55% of PCa is hypoechoic, 5% is hyperechoic, and 40% is isoechoic, these poor sensitivities and specificities are expected due to the inconsistent and nonspecific signature of PCa in TRUS B-mode (Heijmink et al., 2011).

To bolster the performance of TRUS guided biopsy, additional imaging modalities which are more sensitive and specific for PCa can be combined with TRUS B-mode to enhance lesion detectability. Two such techniques are multiparametric magnetic resonance imaging (mp-MRI) fusion biopsy and contrast enhanced ultrasound (CEUS). In mp-MRI fusion biopsy, a previously acquired mp-MRI scan of the patient's prostate is registered with live B-mode during biopsy which allows the clinician to target mp-MRI detected lesions. This technique results in sensitivities of 85-93% and specificities of 41-49% (Siddiqui et al., 2015; Ahmed et al., 2017). CEUS requires a microbubble injection prior to TRUS B-mode imaging and examines the bubble dynamics as they perfuse through the prostate. The microbubble perfusion leads to an increase in PCa detection as the vasculature differs between healthy prostate tissue and PCa. CEUS has a reported sensitivity of 73% and specificity of 58% (Halpern, 2006; Postema et al., 2016). Both techniques have proven to outperform TRUS B-mode but require increased resources, additional physician time, and, for CEUS, a contrast agent injection.

Additional ultrasonic techniques that do not require extra resources to enhance PCa contrast are acoustic radiation force impulse (ARFI) imaging and shear wave elasticity imaging (SWEI). ARFI and SWEI both assess the mechanical properties of the tissue using an acoustic radiation force impulse (ARFI) excitation to displace tissue at the focus of the pushing beam and observe either the on-axis displacement and recovery (ARFI imaging) or the shear wave induced by the pushing beam (SWEI) (Doherty et al., 2013). ARFI imaging

captures a relative measure of tissue stiffness and has been demonstrated to identify 71% of clinically significant PCa with a positive predictive value of 95% (Palmeri et al., 2016). SWEI assesses the shear wave propagation speed (SWS) which, under the assumption that the material is linear, isotropic, incompressible, and elastic, can be used to calculate the Young's modulus (E) as shown in Eqn. 1, where the tissue density (ρ) is assumed to be 1000 kg/m^3.

$$E = 3\rho SWS^2 \quad (1)$$

These Young's moduli provide a quantitative estimate of the tissue stiffness and have demonstrated success in PCa identification (Barr et al., 2012; Rosenzweig et al., 2012; Rouvière et al., 2017; Wei et al., 2018). The Aixplorer system, developed by Supersonic Imagine, is an end-fire TRUS SWEI 2D system that has been used in several studies to establish stiffness thresholds to separate PCa from healthy prostate tissue. Reported Young's modulus thresholds for identifying PCa range from 35 to 82.6 kPa with sensitivities ranging from 53 to 96% and specificities ranging from 66 to 96% (Barr et al., 2012; Correas et al., 2013, 2015; Woo et al., 2014; Rouvière et al., 2017; Wei et al., 2018). This system relies on the clinician's ability to both remain still during data acquisition (3-5 seconds per frame (Barr et al., 2012)) and maintain uniform, minimal compression throughout the acquisition.

Compression needs to be controlled in SWEI and ARFI as soft tissues are known to be inherently nonlinear (Shiina et al., 2015). This material nonlinearity leads to a stiffening of the material with increasing applied strain, and therefore increased SWS estimates with increased compression (Barr and Zhang, 2012; Vachutka et al., 2018). Addressing compression is actively being explored in the field of elasticity imaging. Barr and Zhang assessed compression in breast imaging and used a structure in the far field of the B-mode image to approximate and account for the compression used during imaging (Barr and Zhang, 2012). Woo et al., while assessing PCa, used the ratio of the measured SWS in each suspicious location to the SWS of a non-cancerous prostate region to normalize for compression (Woo et al., 2014). As these approaches appear promising, herein we employ a normalization factor from the mean SWS of the entire prostate and apply it to the measured SWS value at each voxel to account for differences in compression.

In this work, we have developed a 3D TRUS/ARFI/SWEI imaging system with which we have acquired *in vivo* data in patients with biopsy-confirmed PCa who underwent radical prostatectomy immediately following ultrasound imaging. We use whole mount histology data to guide the identification of PCa in the SWEI data to establish a SWS threshold which separates PCa from healthy prostate tissue. We also explore a SWS normalization approach to account for both compression and patient to patient variability. The goal of this work is to demonstrate a 3D data acquisition system for acquiring SWEI data *in vivo* and to establish a stiffness threshold to separate PCa from healthy prostatic tissue to facilitate patient imaging, PCa identification and localization, and the performance of targeted biopsy in a single clinic visit.

Materials and Methods

Data Acquisition

3D TRUS B-mode, ARFI, and SWEI data were acquired in 36 patients who had PCa and were treated with radical prostatectomy immediately following imaging. These patients were in an IRB-approved study and provided written informed consent. Imaging was performed with a modified Siemens SC2000 Scanner (Siemens Medical Solutions, Issaquah, WA, USA) in the operating room with the patient in a dorsal lithomy position and under general anesthesia. Throughout the course of this study, the transducer was updated to the latest available technology. As such, 26 patients were imaged with an ACUSON ER7B transducer, and 10 patients were imaged with a custom designed transrectal Siemens 12L4 transducer. Additionally, these transrectal, side-fire, transducers were placed in a CIVCO Micro-Touch stabilizer and rotation stage (CIVCO Medical Solutions, Kalona, IA, USA). The rotation stage was used to acquire 100 to 150 sagittal images of the prostate with a 1-1.5 degree angular spacing. This data acquisition setup was previously described by Palmeri et al. and Morris et al. (Palmeri et al., 2016; Morris et al., 2020). The prostate was imaged twice, first with a combined ARFI and SWEI sequence and then with a B-mode imaging sequence for a combined acquisition time of approximately 14 minutes. These ARFI, SWEI, and B-mode data are inherently co-registered as the transducer was only adjusted using the mechanical rotation stage during the acquisition. 3-D Slicer (slicer.org) was used to visualize the data with a 0.15 x 0.15 x 0.15 mm^3 voxel size following scan conversion (Fedorov et al., 2012).

The ARFI and SWEI combined sequence is summarized in Tables 1 and 2 (Palmeri et al., 2016; Morris et al., 2020). A multi-focal-zone ARF push excitation was used with three foci (15, 22.5, and 30 mm) to elongate the depth of field and attempt to image the entirety of the prostate (Rosenzweig et al., 2015). Displacement tracking was performed using 16:1 parallel receive tracking. Four beams were located inside the ARF excitation to measure the ARFI displacements and the remaining twelve track lines were separated into two groups of six which were placed on either side of the push beam and used to track the shear wave propagation for SWEI. These two groups of six SWEI tracking lines were laterally offset from the push and spaced 0.76 mm apart for the ER7B and 0.78 mm apart for the 12L4 (Table 2) (Rosenzweig et al., 2012). The slight differences between the ER7B and 12L4 sequences, noted in Tables 1 and 2, are not anticipated to impact the results. The tracking lines were repeated through time to acquire the backscattered signal associated with the tissue's displacement and recovery. These signals were captured as baseband in-phase and quadrature (IQ) data which allows the 5.0 MHz center frequency backscattered signal to be sampled at much lower frequencies. To acquire a fully sampled sagittal image, the ARF push and tracking ensemble was repeated 82 times across the face of the transducer with a spacing of 0.68 mm to generate a 55.76 mm lateral field of view (Table 1).

Data Processing

ARFI Processing: The particle displacement was calculated using Loupas' phase shift estimator on the IQ data corresponding to the tracking lines (Loupas et al., 1995). This estimator calculates the particle velocity progressively through time. A correlation coefficient threshold of 0.98 was used to remove poor estimates. These particle velocities are

then integrated through time to determine the displacement through time profile used for ARFI imaging. Additionally, depth dependent gain was applied to the data to account for the distribution of push excitation strength caused by attenuation and the focal configuration, and histogram equalization was applied to enhance the lesion visibility (Palmeri et al., 2015).

SWEI Processing: The particle velocity through time curves were calculated in the same way as the ARFI data, applying the phase shift estimator to the twelve offset tracking lines. As described by Morris et al. (Morris et al., 2020), techniques developed by Manduca et al. (Manduca et al., 2003), Lipman et al. (Lipman et al., 2016), Song et al. (Song et al., 2014), and Chan et al. (Chan et al., 2018), were used to calculate the shear wave speeds from the particle velocity curves. Briefly, these curves were low pass filtered with a cutoff frequency of 1.5 kHz using a 2^{nd}-order, phase-preserving Butterworth filter. The data were then directionally filtered in the temporal, lateral, and axial dimensions to suppress reflected waves due to the complex structure of the prostate (Lipman et al., 2016). Additionally, these filtered shear waves were temporally aligned with the shear waves generated by consecutive, adjacent ARF excitations to extend the lateral observation window across the entire field of view (Chan et al., 2018). This approach leads to a larger shear wave reconstruction window, which provides additional SWS estimates at each overlapping sample while maintaining high shear wave SNR because energy from each ARF push is only monitored across a distance of 2-7 mm from each excitation. Shear wave speeds were calculated using a 2D vector tracking (axial and lateral directions) approach to accurately estimate the speed at each location (Song et al., 2014). Lastly, the overlapping SWS estimates at each lateral and axial position were averaged to improve SWS SNR and a SWS threshold of 12 m/s along with an empirically chosen correlation coefficient threshold of 0.7 were applied to discard spurious estimates (Chan et al., 2018).

B-mode Processing: The B-mode acquisition for both transducers consisted of 126 focused transmits spanning the 55 mm field of view. An F/3 transmit configuration was used with a 7.0 MHz center frequency along with F/1 dynamic receive focusing (Palmeri et al., 2016). Coherent beamforming and 7:1 parallel receive tracking was used to generate the B-mode IQ data (Loftman, 2017). Also, for both transducers, based 10 logarithmic compression, and median filtering, with a kernel size of 0.25 mm axially and 0.5 mm laterally, were applied to the B-mode data prior to scan conversion.

Histology

The prostates were radically excised immediately following ultrasound imaging, sliced every 3 mm from apex to base, and whole mounted on slides. These slides were hematoxylin and eosin (H&E) stained for analysis by board-certified pathologists. The pathologists identified the locations and Gleason Grade Group (GG) of each PCa foci. Clinically significant PCa foci were identified as having a GG ≥ 2 (Gleason Score 3+4=7) or by being larger than 0.5 mL (Weinreb et al., 2016; Epstein et al., 2016). To assess clinical significance in GG1 (Gleason Score 3+3=6) PCa foci, the volumes of the PCa foci were calculated using the triaxial measurements made by the pathologists and the assumption that they were ellipsoidal and compared to the threshold of 0.5 mL. Regions of benign prostatic hyperplasia

(BPH) and atrophy were also noted by the pathologists. Due to differences in slice thickness and slice angle, these pathology slides were not registered with the ultrasound data (Palmeri et al., 2015, 2016). Instead, the center of each PCa lesion was identified as within one of 27 anatomic regions of interest (Dickinson et al., 2011). The identified region of interest was then used to direct the examination of the ultrasound imaging volumes.

Prostate Segmentation and Value Extraction

TRUS B-mode imaging was used to identify and segment the prostate capsule as B-mode provides clear contrast between the prostate and the surrounding tissue. ARFI imaging was used to identify and segment the central gland (CG) as it is stiffer than the surrounding peripheral zone (PZ). The CG represents the combined transition zone and central zone (Engelbrecht et al., 2003; Futterer and Barentsz, 2009). The capsule and CG segmentations were then extended onto the co-registered SWEI volume and used, along with the histologically determined region of interest corresponding to the ground truth location for each clinically signifcant PCa foci, to identify and segment suspicious regions as PCa in the SWEI volume. The voxels which were included in the capsule segmentation but not the CG or PCa segmentations were labeled as PZ. Mean SWS values were extracted from each region labeled as PZ, CG, and PCa for each prostate. Data visualization and segmentation was performed using 3-D Slicer (slicer.org) (Fedorov et al., 2012). Sample patient data volumes and segmentations are included in Figure 1. Additionally, the mean was calculated from all voxels within the prostate capsule and was used to normalize the means associated with each prostate region. The mean SWS from the entire prostate was used as a normalization factor because it provides an indication of the compression (i.e., initial strain state) applied to the prostate. This process accounts for differences in SWS based on prostate compression and patient-to-patient variability.

Statistical Analysis

The SWS values representing each region are reported as mean ± standard deviation across patients. Regional SWS comparisons were made using three-way repeated measures analysis of variance (ANOVAs) to separate the regional impact of SWS from the presence of benign prostatic hyperplasia (BPH) and from variance introduced by the ultrasound transducer. An additional two-way ANOVA was used to examine the relationship between measured SWS within PCa foci, their corresponding GG (excluding GG5 as this dataset only included 1 GG5 lesion), and the lesion volume. These ANOVAs were performed using JMP Pro 15 (SAS Institute Inc, Cary, NC, USA). Follow-up paired t-tests to identify significant differences between prostate regions were performed using MATLAB R2016b (MathWorks, Natick, MA, USA). Finally, thresholds were generated using Scikit-learn's (scikit-learn.org) version 0.23.1 (Pedregosa et al., 2011) roc_curve and auc packages. The receiver operating characteristic (ROC) curve was established using the roc_curve package, and the area under the receiver operating characteristic (AUC) curve was calculated using the auc package in order to assess the performance of the chosen threshold. The threshold used to separate PCa from healthy tissue (regions identified as PZ or CG) was chosen by maximizing the Youden index (Youden, 1950). Statistical significance was determined using $p<0.05$.

Results

Figure 1 demonstrates the segmentation and PCa identification of a sample prostate with a GG 3 (Gleason 4+3=7) lesion. The axial histology slide approximately corresponding to the axial SWEI image slice shown in Fig 1D is included in Figure 1A, where the prostate capsule is marked in black and the PCa is indicated in purple (Gleason pattern 4) and green (Gleason pattern 3). An *in vivo* TRUS B-mode axial image is included in subplot B and an *in vivo* ARFI axial image is included in subplot C, where the prostate capsule is indicated in green, the CG in black, and the PCa in purple. Subplot D contains the corresponding *in vivo* SWEI axial image, and subplot E contains the *in vivo* SWEI coronal image that bisects the lesion along the dashed black line in subplot D, along with the capsule, CG, and PCa segmentations. The region identified as PZ is within the capsule segmentation (green) and outside the CG (black) and PCa (purple) segmentations. Additionally, Subplot F contains a 3D visualization of the segmented prostate capsule (green) and PCa identified in purple (red arrow).

Figure 2 includes boxplots which capture the mean SWS values for each region of the prostate for each patient included in the study (n = 36). The mean SWS in each region is: 4.8 m/s (69.1 kPa) in the PZ, 5.3 m/s (84.3 kPa) in the CG, and 6.0 m/s (108.0 kPa) for PCa. The prostate region is the only statistically significant ($p<0.05$) factor that was identified by the 3-way repeated measures ANOVA that influences the SWS; the presence of BPH and the use of the two different transducers did not influence SWS. Paired t-testing also determined that the SWS values measured in the different prostate regions were significantly different ($p<0.0001$).

Figure 3 indicates the SWS values found in different grade group lesions. Cancerous SWSs range from 4.1 m/s to 7.7 m/s. The number of cancerous regions is indicated for each grade group. No statistically significant ($p<0.05$) difference was found between any combination of grade groups. Additionally, no statistically significant ($p<0.05$) trend was identified between PCa lesion volume and grade group.

Figure 4 includes boxplots of the mean SWS ratios–the SWS of each voxel normalized by the mean prostate SWS–for each region of the prostate for each patient included in the study (n = 36). The mean ratio of PZ to the entire prostate is 0.95, CG to the entire prostate is 1.05, and PCa to the entire prostate is 1.18. Once again, the prostate region was the only statistically significant ($p<0.05$) factor that was identified by the 3-way repeated measures ANOVA that influences the SWS, and paired t-testing determined that the ratios calculated for each region were statistically significantly different ($p<0.0001$).

Figure 5 indicates the SWS ratio values found in different grade group lesions. Cancerous SWS ratios range from 0.93 to 1.61. As in Fig. 3, The number of cancerous regions is indicated for each grade group. No statistically significant ($p<0.05$) difference was found between any combination of grade groups. Additionally, no statistically significant ($p<0.05$) trend was identified between PCa lesion volume and grade group.

Figure 6 includes the ROC curves for both the SWS mean approach (blue) and the SWS ratio approach (orange) which are made to separate PCa from both PZ and CG. The SWS

that maximized the Youden index for the SWS mean approach was a threshold of 5.6 m/s (94.1 kPa) with a resulting AUC of 0.84. The SWS ratio which maximized the Youden index for the SWS ratio approach was 1.11 with an AUC of 0.90. Additionally, the ROC curves for the histogram equalized ARFI data and the histogram equalized ARFI ratio approach when used to separate PCa from PZ and CG are included in green and red, respectively. The ARFI threshold which maximized the Youden index for the general approach was 104 and yielded an AUC of 0.80. The ARFI ratio threshold which maximized the Youden index was 0.94 with an AUC of 0.85. These results are included in Table 3, along with the positive predictive value (PPV), negative predictive value (NPV), sensitivity, and specificity. Note an increased PPV for the normalized SWS ratio approach with only a minor decrease in NPV, and an increased specificity for the normalized SWS ratio approach with a corresponding decrease in sensitivity compared to the SWS results, and similar improvements to the PPV, NPV, and sensitivity for the ARFI ratio compared to the general histogram equalized ARFI data.

Figure 7 is a scatterplot of mean histogram equalized ARFI value versus mean SWS for each prostate region (PZ indicated by circles, CG indicated by asterisks, and PCa indicated by triangles). This data yields a weak negative correlation ($R^2 = 0.40$). Note the PCa is more localized toward high SWS and lower ARFI histogram equalized values.

Discussion

PCa has been reported as stiffer than benign tissue in the literature, with cutoff values for identifying PCa using Young's Moduli between 35 and 82.6 kPa (Barr et al., 2012; Correas et al., 2013, 2015; Woo et al., 2014; Rouvière et al., 2017; Wei et al., 2018). The boxplot included in Figure 2, indicates that the SWS values corresponding to PCa are statistically significantly ($p>0.0001$) higher than those corresponding to PZ and to CG, which agrees with the literature, though these PCa SWS values are approximately 20% greater than those literature-quoted values (Eqn. 1). Additionally, in the literature, stiffness thresholds for PCa using an end-fire array span from 35 to 49 kPa (Barr et al., 2012; Correas et al., 2013, 2015; Woo et al., 2014; Rouvière et al., 2017) with higher thresholds of 76 kPa and 82.6 kPa being reported using a side-fire array (Rouvière et al., 2017; Wei et al., 2018). As expected, the SWS threshold identified in this work (5.6 m/s, 94.1 kPa) aligns more closely with the side-fire acquired thresholds in the literature, although it is still higher.

One likely contributing factor to this elevated SWS threshold, when compared to other TRUS/SWE side-fire reports in the literature, is that measured SWSs are influenced by differences in shear wave propagation distance and frequency content. Prostate tissue, like all tissues, is viscoelastic (VE). In VE materials, wave propagation is both dispersive, with a frequency dependent shear wave propagation speed, and attenuating, with a frequency dependent amplitude decay with propagation distance (Sridhar et al., 2007; Deffieux et al., 2009; Lipman et al., 2018). In this study, shear wave speeds were measured over a propagation distance from 2.7 - 5.7 mm. Though the technical specifics of the Aixplorer system are not available, it is likely that the shear wave propagation distance is considerably further than used here as its frame rate supports real-time imaging while the framerate in this study is approximately 0.2 Hz. Different propagation distances would be associated with

both a downshift in the relative frequency content present in the Aixplorer system as the shear waves are attenuated over a longer distance, and an increase in the SNR in our system as the amplitude decay caused by the attenuation is reduced across the shorter distance. Additionally, the elevated frequency content of the shear waves analyzed by our system would lead to an increase in the measured shear wave speed as, in dispersive materials, shear waves with higher frequency content are associated with higher measured shear wave speeds (Rouze et al., 2018).

The primary cause of our increased stiffness threshold is likely that our 3D acquisition setup may require additional compression compared to the handheld approach. In the 3D system herein, the transducer is locked into a rotation stage and not adjusted by the user throughout the 14-minute imaging time. Compression is required to maintain adequate coupling between the transducer and the patient's rectal wall throughout the entire 150-degree rotation. This likely increased compression when compared to the handheld reports in the literature which is expected to cause an increase in the stiffness and measured SWS due to the inherent nonlinearity of soft tissues (Barr and Zhang, 2012; Shiina et al., 2015; Vachutka et al., 2018).

Variable transducer compression, along with anatomic variations, can lead to variability in measured SWS not associated with PCa. The patient-to-patient variability complicates establishing a threshold for PCa detection. To address this variability, we investigated a SWS ratio approach, where we divided the mean SWS in the specific regions by the mean SWS of the entire prostate (Figure 4). This approach is similar to the approach used by Woo et al., where SWS regions of interest (ROIs) were placed along biopsy tracts and the reported SWSs from the positive PCa cores were divided by the minimum SWS of the remaining negative cores (Woo et al., 2014). Using this technique, Woo et al., reported a SWS ratio threshold of 3.0 to distinguish PCa from healthy tissue which is considerably higher than the SWS ratio threshold identified in this study of 1.11. This difference in ratios can be attributed to the value used to represent healthy tissue. We used the mean of the entire prostate as this considers the initial strain state of the whole prostate and therefore provides a better internal control. Additionally, using the mean SWS from the entire prostate is an approach that can be readily automated for future studies.

A subset of the literature demonstrates increased SWS with increased grade group (Woo et al., 2014; Correas et al., 2015; Wei et al., 2018; Dai et al., 2020). We did not observe a correlation between grade group and SWS in our data (Figures 3 and 5), however, the distribution of grade groups in subjects receiving prostatectomies at our institution includes few higher grade subjects: our cohort only had 3 patients with GG4 lesions and a single patient with a GG5 lesion.

An additional factor which we considered as a possible confounder for SWS measurements was the presence of BPH, which is an enlargement of the prostate and typically grows in the transition zone (McNeal, 1981). Zheng et al. used the Siemens ACUSON S2000 (Siemens Medical Solutions, Issaquah, WA, USA) to measure SWSs in patients with BPH and PCa and identified elevated SWSs in prostate regions corresponding to BPH (Zheng et al., 2012). While 50% (18 out of 36) of the patients included in this study had both BPH and PCa, the

impact of BPH on the measured SWSs in each region of the prostate was not statistically significant.

Although the reported SWSs are somewhat elevated compared to the literature, the reported SWS and SWS ratio thresholds (Figure 6, Table 3) yield sensitivities (81% and 75%, respectively) and specificities (82% and 90%, respectively) which fall within the range of reported values (53-96% and 66-96%, respectively) (Barr et al., 2012; Correas et al., 2013, 2015; Woo et al., 2014; Rouvière et al., 2017; Wei et al., 2018). Additionally, both thresholds result in lower sensitivities with correspondingly higher specificities than mp-MRI fusion biopsy, where the sensitivity for mp-MRI fusion biopsy is 85-93% and the specificity is 41-49% (Siddiqui et al., 2015; Ahmed et al., 2017). Both the SWS threshold and the SWS ratio threshold also match or outperform CEUS in sensitivity and specificity (73% and 58%, respectively) (Halpern, 2006; Postema et al., 2016). As the goal of this work is to demonstrate the capabilities of SWEI for PCa identification, it may be appropriate to lower the PCa threshold for both the SWS approach and the SWS ratio approach so as to increase the sensitivity, which could lead to the sensitivity and specificity more closely aligning with the current best practices of mp-MRI fusion biopsy.

Along with the thresholds generated using the SWS and SWS ratio approaches, thresholds were created using the histogram equalized ARFI and histogram equalized ARFI ratio values (Figure 6, Table 3). This histogram equalized ARFI threshold of 104 yielded a PPV of 60% and a specificity of 75% which are both lower than the PPV and specificity of the SWS and normalized SWS ratio approaches. The histogram equalized ARFI ratio yielded a threshold of 0.94 with improvements over the general ARFI threshold as the PPV, NPV, sensitivity, and specificity are 65%, 92%, 86%, and 76%. This ARFI ratio yields a lower PPV and specificity than the SWEI thresholds though improves the NPV and sensitivity. In both the SWEI and ARFI comparisons of the normalized ratio approach to the general approach, improvements are evident and indicate that using an entire prostate mean value to normalize either the SWEI or ARFI values to account for compression and patient variability improves the ability of either elasticity metric to identify PCa.

Though the ARFI thresholds herein show promising results, the reported PPV is considerably lower than the 95% reported by Palmeri et al. (Palmeri et al., 2016). One clear reason for the difference between these PPVs is that this study quantitatively assesses ARFI voxel values based on PCa segmentation established using SWEI, instead of utilizing the qualitative metrics (boundary definition, contrast, texture, and location) used by Palmeri et al.. This limitation is supported by our previous work which suggests the qualitative aspects of ARFI are not matched by SWEI, particularly in border definition and local contrast (Morris et al., 2020). This suggests that ARFI and SWEI could be used synergistically to take advantage of the qualitative aspects of ARFI along with the quantitative aspects of SWEI for future PCa screening studies.

To further examine the relationship between ARFI and SWEI, we calculated the correlation between the mean histogram equalized ARFI value for each region and the mean SWS for each region, as seen in Figure 7. The histogram equalized ARFI values and the SWS values proved to be weakly negatively correlated (R^2=0.40). This finding supports using ARFI and

SWEI synergistically to detect PCa as the weak correlation indicates that both imaging techniques provide different information.

There are some limitations to this retrospective analysis associated with both the patient population and the assumptions made during SWS measurement. As previously mentioned, the patients enrolled in this study were undergoing radical prostatectomy, which may bias the specified thresholds toward clinically significant PCa. Additionally, our cohort included only a limited number of patients with high-grade PCa. A limitation associated with SWS measurement is that SWEI relies on a region of assumed homogeneity which is not guaranteed within the prostate as it is a heterogenous gland. While our short shear wave propagation distance and 3D directional filtering improves the reliability of the SWS measurements made over small regions, PCa foci and structures within the prostate which are smaller than our lateral resolution of 1.3 mm cannot be resolved (Chan et al., 2018).

Conclusions

3D SWEI separates PCa from healthy prostate tissue with sensitivities and specificities akin to mp-MRI fusion biopsy. The mean SWS in each prostate region (PZ, CG, and PCa) identified a threshold of 5.6 m/s (94.1 kPa) to separate PCa from healthy tissue with a sensitivity of 81%, specificity of 82%, PPV of 69%, NPV of 89%, and AUC of 0.84. Additionally, we demonstrated improved PCa detection performance by accounting for differences in tissue compression and patient variability during acquisition by normalizing the SWS by the mean SWS in the entire prostate. This approach yields a SWS ratio threshold of 1.11 to separate PCa from healthy prostate tissue and is accompanied by a substantial increase in specificity, PPV, and AUC, with a specificity of 90%, PPV of 79%, and AUC of 0.90. This work demonstrates the feasibility of using 3D SWEI data in a PCa screening system and the benefits of normalizing for applied compression during data acquisition and paves the way for future SWEI targeted biopsy studies.

Acknowledgements

This work was supported by National Institutes of Health (NIH) Grants R01 CA142824, and T32-EB001040 and Department of Defense (DoD) Grant USAMRMC award number W81XWH-16-1-0653. The authors thank Siemens Medical Solutions USA, Inc., Ultrasound, for their in-kind technical support.

References

Ahmed HU, El-Shater Bosaily A, Brown LC, Gabe R, Kaplan R, Parmar MK, Collaco-Moraes Y, Ward K, Hindley RG, Freeman A, Kirkham AP, Oldroyd R, Parker C, Emberton M. Diagnostic accuracy of multi-parametric MRI and TRUS biopsy in prostate cancer (PROMIS): a paired validating confirmatory study. The Lancet, 2017;389:815–822.

Barr RG, Memo R, Schaub CR. Shear wave ultrasound elastography of the prostate: Initial results. Ultrasound Quarterly, 2012;28:13–20. [PubMed: 22357224]

Barr RG, Zhang Z. Effects of Precompression on Elasticity Imaging of the Breast. Journal of Ultrasound in Medicine, 2012;31:895–902. [PubMed: 22644686]

Chan DY, Lipman SL, Palmeri ML, Morris DC, Polascik TJ, Rouze NC, Nightingale KR. Prostate Shear Wave Elastography: Multiresolution Reconstruction Dependence on Push Beam Spacing. In: IEEE International Ultrasonics Symposium, IUS. Vol. 2018-1. IEEE Computer Society, 2018.

Correas J, Tissier A, Khairoune A. Ultrasound elastography of the prostate : State of the art. Diagnostic and Interventional Imaging, 2013;94:551–560. [PubMed: 23607924]

Correas JM, Tissier AM, Khairoune A, Vassiliu V, Méjean A, Hélénon O, Memo R, Barr RG. Prostate cancer: Diagnostic performance of real-time shear-wave elastography. Radiology, 2015;275:280–289. [PubMed: 25599156]

Dai WB, Xu J, Yu B, Chen L, Chen Y, Zhan J. Correlation of Stiffness of Prostate Cancer Measured by Shear Wave Elastography with Grade Group: A Preliminary Study. Ultrasound in Medicine and Biology, 2020.

Deffieux T, Montaldo G, Tanter M, Fink M. Shear wave spectroscopy for in vivo quantification of human soft tissues visco-elasticity. IEEE Trans Med Imaging, 2009;28:313–322. [PubMed: 19244004]

Dickinson L, Ahmed HU, Allen C, Barentsz JO, Carey B, Futterer JJ, Heijmink SW, Hoskin PJ, Kirkham A, Padhani AR, Persad R, Puech P, Punwani S, Sohaib AS, Tombal B, Villers A, Van Der Meulen J, Emberton M. Magnetic resonance imaging for the detection, localisation, and characterisation of prostate cancer: Recommendations from a European consensus meeting. European Urology, 2011;59:477–494. [PubMed: 21195536]

Doherty JR, Trahey GE, Nightingale KR, Palmeri ML. Acoustic radiation force elasticity imaging in diagnostic ultrasound. IEEE Transactions on Ultrasonics, Ferroelectrics, and Frequency Control, 2013;60:685–701.

Engelbrecht MR, Huisman HJ, Laheij RJ, Jager GJ, Van Leenders GJ, Hulsbergen-Van De Kaa CA, De la Rosette JJ, Blickman JG, Barentsz JO. Discrimination of prostate cancer from normal peripheral zone and central gland tissue by using dynamic contrast-enhanced MR imaging. Radiology, 2003;229:248–254. [PubMed: 12944607]

Epstein JI, Zelefsky MJ, Sjoberg DD, Nelson JB, Egevad L, Magi-Galluzzi C, Vickers AJ, Parwani AV, Reuter VE, Fine SW, Eastham JA, Wiklund P, Han M, Reddy CA, Ciezki JP, Nyberg T, Klein EA. A Contemporary Prostate Cancer Grading System: A Validated Alternative to the Gleason Score. European Urology, 2016;69:428–435. [PubMed: 26166626]

Fedorov A, Beichel R, Kalpathy-Cramer J, Finet J, Fillion-Robin JC, Pujol S, Bauer C, Jennings D, Fennessy F, Sonka M, Buatti J, Aylward S, Miller JV, Pieper S, Kikinis R. 3D Slicer as an image computing platform for the Quantitative Imaging Network. Magnetic Resonance Imaging, 2012;30:1323–1341. [PubMed: 22770690]

Futterer JJ, Barentsz JO. 3T MRI of prostate cancer. Applied Radiology, 2009;38:25+.

Halpern EJ. Contrast-enhanced ultrasound imaging of prostate cancer. Reviews in urology, 2006;8 Suppl 1:S29–S37. [PubMed: 17021624]

Heijmink SW, Fütterer JJ, Strum SS, Oyen WJ, Frauscher F, Witjes JA, Barentsz JO. State-of-the-art uroradiologic imaging in the diagnosis of prostate cancer. Acta Oncologica, 2011;50:25–38.

Lipman SL, Rouze NC, Palmeri ML, Nightingale KR. Evaluating the improvement in shear wave speed image quality using multidimensional directional filters in the presence of reflection artifacts. IEEE Transactions on Ultrasonics, Ferroelectrics, and Frequency Control, 2016;63:1049–1063.

Lipman SL, Rouze NC, Palmeri ML, Nightingale KR. Impact of Acoustic Radiation Force Excitation Geometry on Shear Wave Dispersion and Attenuation Estimates. Ultrasound in Medicine and Biology, 2018;44:897–908. [PubMed: 29422328]

Loftman R IN Focus Coherent Technology. Tech. rep., Siemens Healthcare, 2017.

Loupas T, Peterson RB, Gill RW. Experimental Evaluation of Velocity and Power Estimation for Ultrasound Blood Flow Imaging, by Means of a Two-Dimensional Autocorrelation Approach. IEEE Transactions on Ultrasonics, Ferroelectrics, and Frequency Control, 1995;42:689–699.

Manduca A, Lake DS, Kruse SA, Ehman RL. Spatio-temporal directional filtering for improved inversion of MR elastography images. Medical Image Analysis, 2003;7:465–473. [PubMed: 14561551]

McNeal JE. The zonal anatomy of the prostate. The Prostate, 1981;2:35–49. [PubMed: 7279811]

Morris DC, Chan DY, Lye TH, Chen H, Palmeri ML, Polascik TJ, Foo WC, Huang J, Mamou J, Nightingale KR. Multiparametric Ultrasound for Targeting Prostate Cancer: Combining ARFI, SWEI, QUS and B-Mode. Ultrasound in Medicine and Biology, 2020;46:3426–3439. [PubMed: 32988673]

Mottet N, Bellmunt J, Bolla M, Briers E, Cumberbatch MG, De Santis M, Fossati N, Gross T, Henry AM, Joniau S, Lam TB, Mason MD, Matveev VB, Moldovan PC, van den Bergh RCN, Van den Broeck T, van der Poel HG, van der Kwast TH, Rouvière O, Schoots IG, Wiegel T, Cornford P. EAU-ESTRO-SIOG Guidelines on Prostate Cancer. Part 1: Screening, Diagnosis, and Local Treatment with Curative Intent. European Urology, 2017;71:618–629. [PubMed: 27568654]

Palmeri ML, Glass TJ, Miller ZA, Rosenzweig SJ, Buck A, Polascik TJ, Gupta RT, Brown AF, Madden J, Nightingale KR. Identifying Clinically Significant Prostate Cancers using 3-D In Vivo Acoustic Radiation Force Impulse Imaging with Whole-Mount Histology Validation. Ultrasound in Medicine and Biology, 2016;42:1251–1262. [PubMed: 26947445]

Palmeri ML, Miller ZA, Glass TJ, Garcia-Reyes K, Gupta RT, Rosenzweig SJ, Kauffman C, Polascik TJ, Buck A, Kulbacki E, Madden J, Lipman SL, Rouze NC, Nightingale KR. B-mode and acoustic radiation force impulse (ARFI) imaging of prostate zonal anatomy: Comparison with 3T T2-weighted MR imaging. Ultrasonic Imaging, 2015;37:22–41. [PubMed: 25060914]

Pedregosa F, Varoquaux G, Gramfort A, Michel V, Thirion B, Grisel O, Blondel M, Prettenhofer P, Weiss R, Dubourg V, Vanderplas J, Passos A, Cournapeau D, Brucher M, Perrot M, Duchesnay E. Scikit-learn: Machine Learning in Python. Journal of Machine Learning Research, 2011;12:2825–2830.

Postema A, Mischi M, de la Rosette J, Wijkstra H. Multiparametric ultrasound in the detection of prostate cancer: a systematic review. World Journal of Urology, 2015;33:1651–1659. [PubMed: 25761736]

Postema AW, Frinking PJ, Smeenge M, De Reijke TM, De La Rosette JJ, Tranquart F, Wijkstra H. Dynamic contrast-enhanced ultrasound parametric imaging for the detection of prostate cancer. BJU International, 2016;117:598–603. [PubMed: 25754526]

Rosenzweig S, Palmeri M, Nightingale K. Analysis of rapid multi-focal-zone ARFI imaging. IEEE Transactions on Ultrasonics, Ferroelectrics, and Frequency Control, 2015;62:280–289.

Rosenzweig S, Palmeri M, Rouze N, Lipman S, Kulbacki E, Madden J, Polascik T, Nightingale K. Comparison of concurrently acquired in vivo 3D ARFI and SWEI images of the prostate. In: IEEE International Ultrasonics Symposium, IUS, 2012. pp. 97–100.

Rouvière O, Melodelima C, Hoang Dinh A, Bratan F, Pagnoux G, Sanzalone T, Crouzet S, Colombel M, Mège-Lechevallier F, Souchon R. Stiffness of benign and malignant prostate tissue measured by shear-wave elastography: a preliminary study. European Radiology, 2017;27:1858–1866. [PubMed: 27553936]

Rouze NC, Deng Y, Trutna CA, Palmeri ML, Nightingale KR. Characterization of Viscoelastic Materials Using Group Shear Wave Speeds. IEEE Transactions on Ultrasonics, Ferroelectrics, and Frequency Control, 2018;65:780–794.

Shiina T, Nightingale KR, Palmeri ML, Hall TJ, Bamber JC, Barr RG, Castera L, Choi BI, Chou YH, Cosgrove D, Dietrich CF, Ding H, Amy D, Farrokh A, Ferraioli G, Filice C, Friedrich-Rust M, Nakashima K, Schafer F, Sporea I, Suzuki S, Wilson S, Kudo M. WFUMB guidelines and recommendations for clinical use of ultrasound elastography: Part 1: Basic principles and terminology. Ultrasound in Medicine and Biology, 2015;41:1126–1147. [PubMed: 25805059]

Siddiqui MM, Rais-Bahrami S, Turkbey B, George AK, Rothwax J, Shakir N, Okoro C, Raskolnikov D, Parnes HL, Linehan WM, Merino MJ, Simon RM, Choyke PL, Wood BJ, Pinto PA. Comparison of MR/ultrasound fusion-guided biopsy with ultrasound-guided biopsy for the diagnosis of prostate cancer. JAMA - Journal of the American Medical Association, 2015;313:390–397. [PubMed: 25626035]

Siegel RL, Miller KD, Jemal A. Cancer statistics, 2020. CA: A Cancer Journal for Clinicians, 2020;70:7–30. [PubMed: 31912902]

Song P, Manduca A, Zhao H, Urban MW, Greenleaf JF, Chen S. Fast shear compounding using robust 2-d shear wave speed calculation and multi directional filtering. Ultrasound in Medicine and Biology, 2014;40:1343–1355. [PubMed: 24613636]

Sridhar M, Liu J, Insana MF. Viscoelasticity imaging using ultrasound: parameters and error analysis. Physics in Medicine and Biology, 2007;52:2425–2443. [PubMed: 17440244]

Vachutka J, Sedlackova Z, Furst T, Herman M, Herman J, Salzman R, Dolezal L. Evaluation of the Effect of Tissue Compression on the Results of Shear Wave Elastography Measurements. Ultrasonic Imaging, 2018;40:380–393. [PubMed: 30101677]

Wei C, Li C, Szewczyk-Bieda M, Upreti D, Lang S, Huang Z, Nabi G. Performance Characteristics of Transrectal Shear Wave Elastography Imaging in the Evaluation of Clinically Localized Prostate Cancer: A Prospective Study. Journal of Urology, 2018;200:549–558.

Weinreb JC, Barentsz JO, Choyke PL, Cornud F, Haider MA, Macura KJ, Margolis D, Schnall MD, Shtern F, Tempany CM, Thoeny HC, Verma S. PI-RADS Prostate Imaging - Reporting and Data System: 2015, Version 2. European Urology, 2016;69:16–40. [PubMed: 26427566]

Woo S, Kim SY, Cho JY, Kim SH. Shear wave elastography for detection of prostate cancer: A preliminary study. Korean Journal of Radiology, 2014;15:346–355. [PubMed: 24843239]

Youden WJ. Index for rating diagnostic tests. Cancer, 1950;3:32–35. [PubMed: 15405679]

Zheng X, Ji P, Mao H, Hu J. A comparison of virtual touch tissue quantification and digital rectal examination for discrimination between prostate cancer and benign prostatic hyperplasia. Radiology and Oncology, 2012;46:69–74. [PubMed: 22933982]

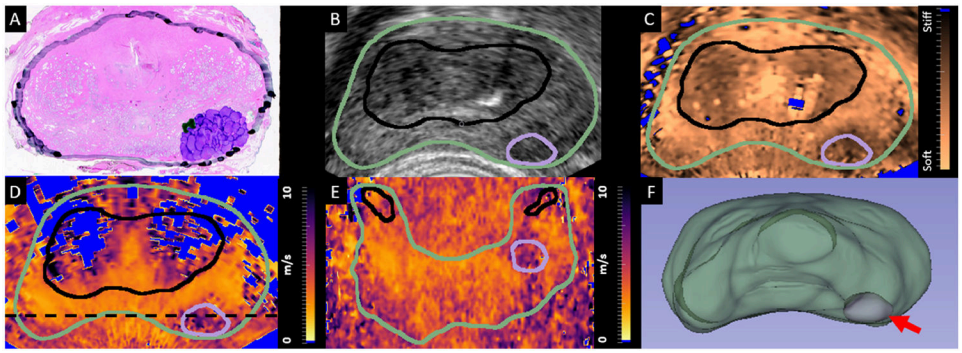

Figure 1:

The axial histology slide corresponding to the center of a Gleason grade group 3 (Gleason 4+3=7) PCa foci, with the prostate capsule (black), Gleason pattern 4 PCa (purple), and Gleason pattern 3 PCa (green) also indicated. B. TRUS *in vivo* axial B-mode image from the matched region in the prostate which was used to identify and segment the prostate capsule (green). C. Matched *in vivo* ARFI axial image which was used to identify and segment the CG (black). D. Matched *in vivo* SWEI axial image indicating both the capsule and CG segmentations along with the PCa segmentation (purple). E. *in vivo* SWEI coronal image corresponding to a plane bisecting the PCa along the dashed black line in D with the capsule (green), CG (black) and PCa (purple) also included. F. 3D visualization of the segmented prostate capsule (green) and PCa (purple, arrow). In subplots C-E, voxels which did not meet the data quality requirements were excluded (blue). PCa = prostate cancer; TRUS = transrectal ultrasound; ARFI = acoustic radiation force impulse; CG = central gland; SWEI = shear wave elasticity imaging;

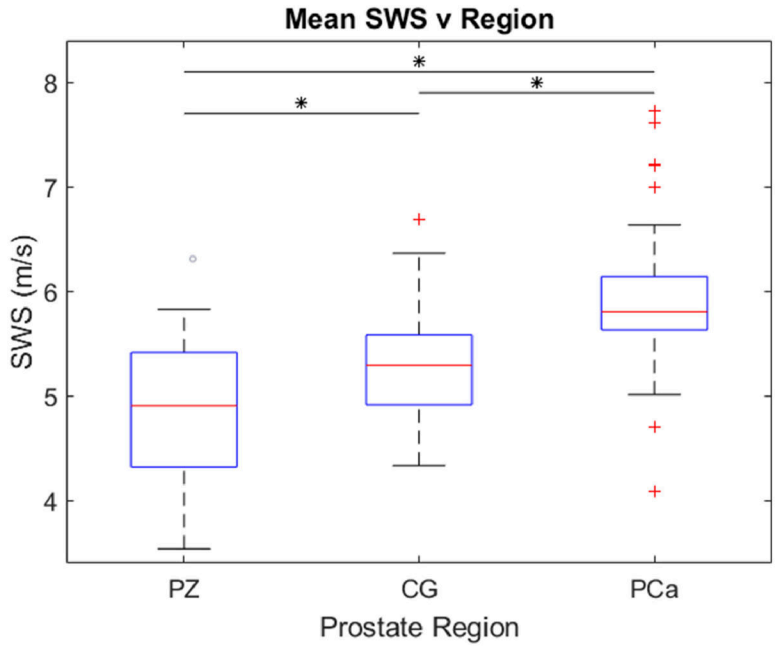

Figure 2:

Boxplots representing the mean SWS values in each prostate versus the prostate region (PZ – peripheral zone; CG – central gland; PCa – segmented prostate cancer). Each column contains data from 36 patients. Statistically significant differences ($p<0.0001$) are indicated by asterisks (*). SWS = shear wave speed.

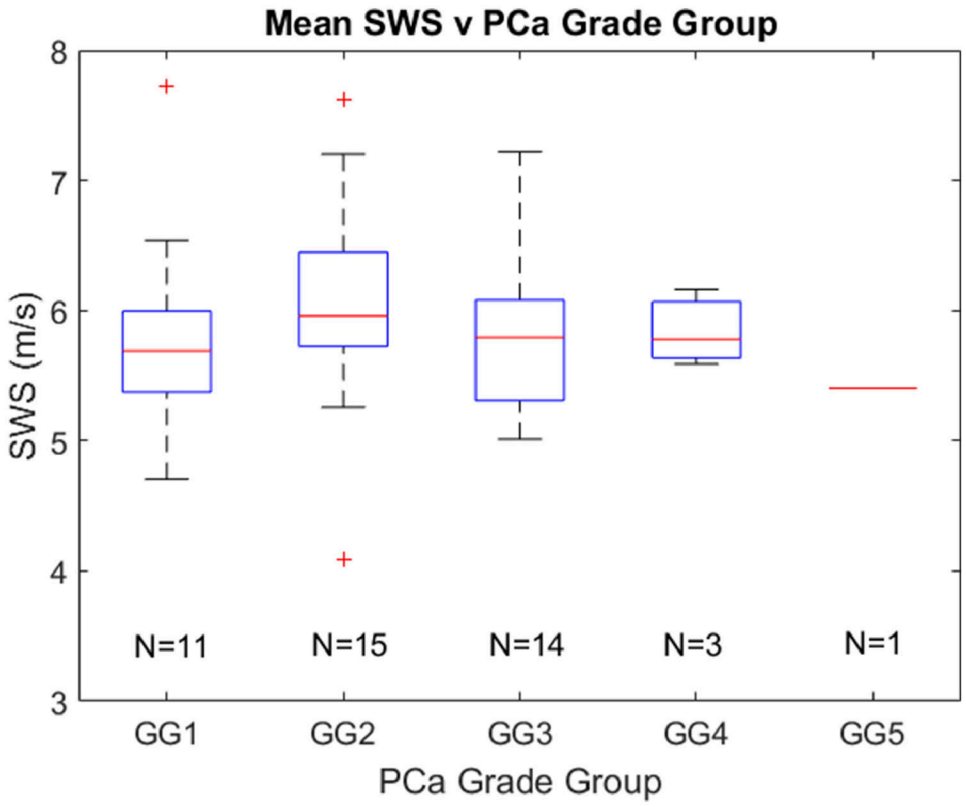

Figure 3:
Boxplots representing the mean SWS values in each PCa foci grouped by Gleason grade group (GG). The number of cancerous regions is indicated for each grade group. No statistically different ($p<0.05$) relationships were identified between grade groups. SWS = shear wave speed.

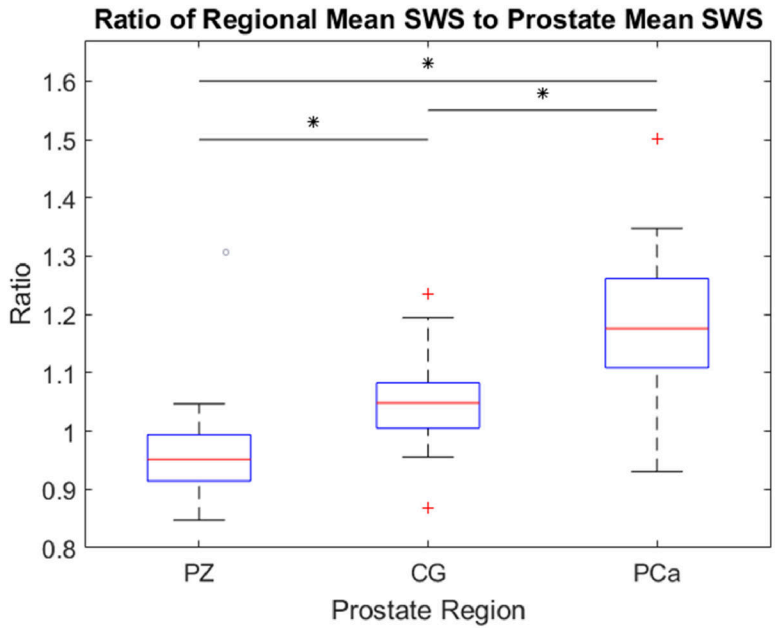

Figure 4:

Boxplots representing the ratio of the regional mean SWS to the entire prostate mean SWS versus the prostate region (PZ – peripheral zone; CG – central gland; PCa – segmented prostate cancer). Each column contains data from 36 patients. Statistically significant differences ($p<0.0001$) are indicated by asterisks (*).

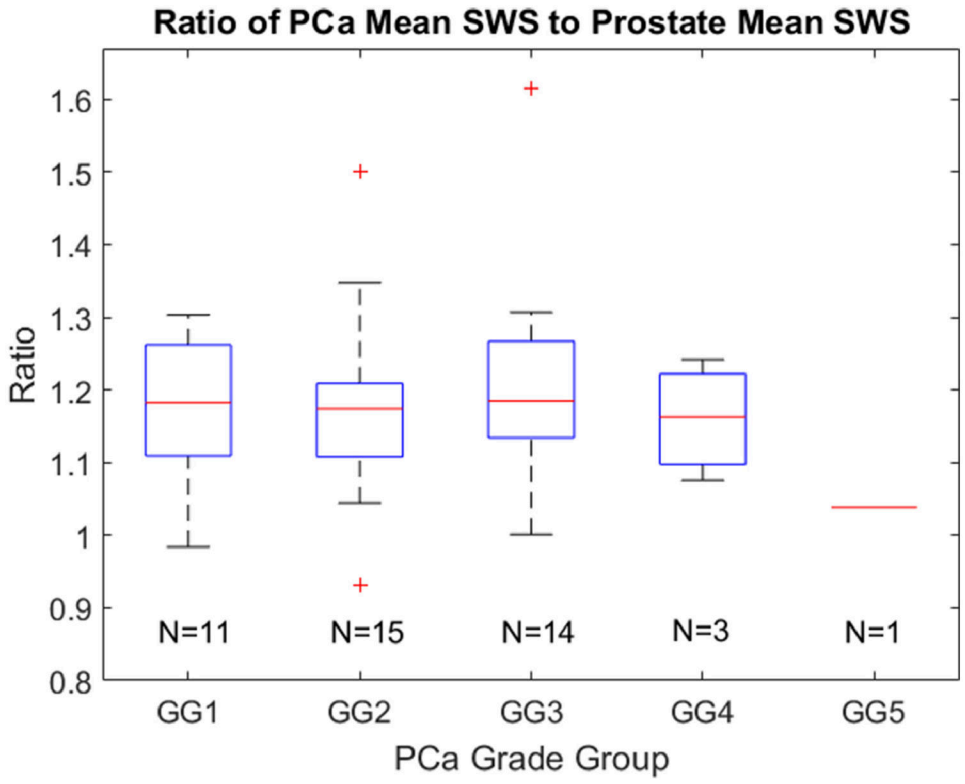

Figure 5:

Boxplots representing the mean SWS ratio values in each PCa foci grouped by Gleason Grade group (GG). The number of cancerous regions is indicated for each grade group. No statistically different ($p<0.05$) relationships were identified between grade groups.

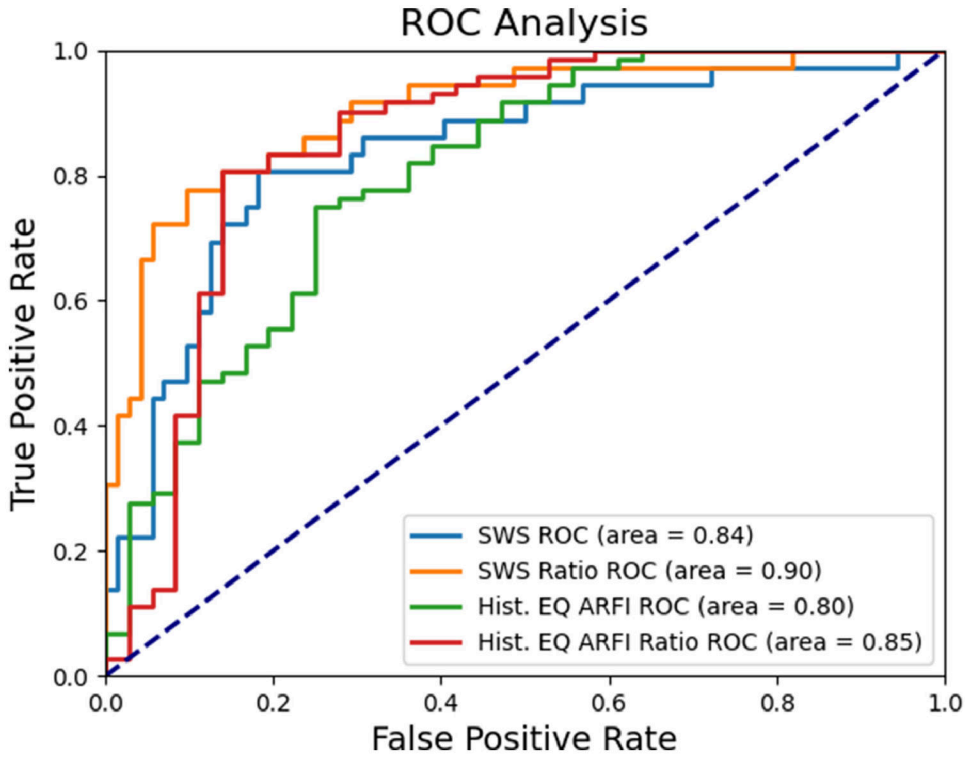

Figure 6:

ROC curves for the SWS mean approach (light blue), the SWS ratio approach (orange), the histogram equalized ARFI (green), and the histogram equalized ARFI ratio (red). Note all ROC curves yield AUCs well above 0.5. The value which maximizes the Youden index for the SWS mean approach is 5.6 m/s, for the SWS ratio approach is 1.11, for the histogram equalized ARFI data is 104, and for the histogram equalized ARFI ratio is 0.94. ROC = receiver operating characteristic; SWS = shear wave speed; Hist. EQ ARFI = histogram equalized acoustic radiation force impulse.

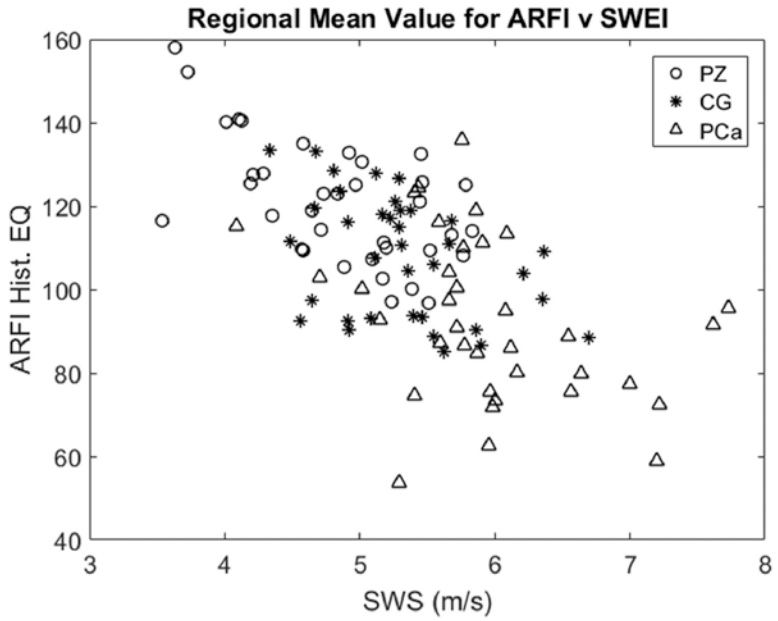

Figure 7:

The mean histogram equalized ARFI values versus the mean SWS values for each prostate region in each patient. SWS = shear wave speed; ARFI Hist. EQ = histogram equalized acoustic radiation force impulse; PZ = peripheral zone; CG = central gland; PCa = prostate cancer.

Table 1:

The ARF push excitation parameters for the ER7B and 12L4 transducers.

Transducer	Transmit Foci (mm)	Frequency (MHz)	Number of Cycles	F-number	Mechanical Index	Push Spacing (mm)	Number of patients
ER7B	30, 22.5, 15	4.6, 4.6, 5.4	300, 300, 300	2.0, 2.0, 2.35	1.09, 1.39, 1.74	0.68	26
12L4	30, 22.5, 15	4.6, 4.6, 4.6	300, 300, 300	2.0, 2.0, 2.0	0.80, 1.09, 1.18	0.68	10

Table 2:

The ARFI/SWEI hybrid tracking configuration for the ER7B and 12L4 transducers.

Transducer	Transmit Focus (mm)	Frequency (MHz)	F-number	PRF (kHz)	ARFI Track Spacing (mm)	SWEI Track Offset (mm)	SWEI Track Spacing (mm)	Track Duration (ms)
ER7B	60	5.0	3.0	8.0	0.17	1.89	0.76	5
12L4	60	5.0	2.0	10.0	0.17	2.01	0.78	4.3

Table 3:

Thresholds determined by maximizing the Youden index of the ROC curves shown in Figure 7, along with the corresponding area under the receiver operating characteristic curve (AUC), positive predictive value (PPV), negative predictive value (NPV), sensitivity, and specificity.

	Threshold	AUC	PPV	NPV	Sensitivity	Specificity
SWS	5.6 m/s	0.84	69%	89%	81%	82%
SWS Ratio	1.11	0.90	79%	88%	75%	90%
Histogram Equalized ARFI	104	0.80	60%	86%	75%	75%
Histogram Equalized ARFI Ratio	0.94	0.85	65%	92%	86%	76%